nature sustainability

Article

https://doi.org/10.1038/s41893-026-01872-1

Respiratory-inspired electrostatic open-microfluidics for air purification

Received: 27 October 2025

Accepted: 13 May 2026

Published online: 22 June 2026

Check for updates

Hanxu Chen (陈涵旭)[1], Ning Li (李宁)[1], Minhui Lu (卢敏慧)[1], Junkai Wang (王俊凯)[1] & Yuanjin Zhao (赵远锦)[1,2]

The human respiratory system can remove most pollutants from inhaled air through the abundance of mucus and cilia on curved airway surfaces. Inspired by such a gas–liquid interface, here we develop an electrostatic open-microfluidics (EOM) system for biomimetic air purification. The EOM system features electrostatic field-assisted polarization and deflection and dynamically refreshed gas–liquid interface of open-microfluidics. Due to the surface energy difference and tailored wettability, particulate pollutants in the air are preferentially captured at the gas–liquid interface, enhanced by extra electric field force. Besides, polarized gaseous pollutants can be activated by free radicals and electrons and removed by customized functional liquids. Additionally, herringbone-like open channels contribute to sufficient interaction between flowing air and liquids, further updating the interface and improving the removal efficiency. The application potential of the EOM system is demonstrated for air purification in domestic scenarios and lung disease prevention. Moreover, the operability and integration capabilities endow the EOM system with application potential for scaled-up industrial exhaust gas purification. Overall, this work provides a viable approach for efficient air purification.

Air pollutants, such as particulate matter (PM) and toxic gases, have a serious impact on human health and daily lives[1–8]. To solve this worsening problem, several strategies have been proposed, including polymer adsorbents, porous filters, interface absorption and so on[9–15]. Benefiting from the simplicity, size-selectivity and low pressure drop, porous filters (for example, monoliths, hollow fibres or 3D-printed microstructures) have been widely applied in various fields[16–21]. However, excessive deposition of pollutants, frequent blockage of filters and ineluctable escape of these pollutants severely limited the further applications of traditional filters or absorbents. Intriguingly, methods based on gas–liquid interface absorption could realize efficient anchoring of pollutants, where the solid particles tend to be captured at the interface due to the surface energy difference between gas–liquid–solid phases[22–28]. This method avoids the excessive contaminant buildup at the filter interface and prolongs the service life. In particular, gas–liquid interface in the form of homogeneous microbubbles has demanded increasing attention, with excellent reusability, reduced overall costs and antifouling performance[29–31]. Although substantial progress has been achieved, the pressure drop derived from discontinuous gas flow remains challenging in different practical scenarios, such as higher resistance, low clean air flow rate or excessive instability. In addition, the static liquid phase easily approaches saturation state and brings further challenges to improving the air purification efficiency. Therefore, advances in purification strategies for the continuous and efficient capture of pollutants are still anticipated.

Here, inspired by the purification function of the human respiratory system, we proposed an electrostatic open-microfluidics (EOM) system for air purification, as shown in Fig. 1. The human respiratory system is composed of curved airways, whose surfaces feature abundant mucus and cilia. The inhaled pollutants are firstly captured from the air by mucus at the gas–liquid interface, and then transported by the dynamically flowing mucus under the action of cilia[32–34]. Taking

[1]Department of Rheumatology and Immunology, Nanjing Drum Tower Hospital, School of Biological Science and Medical Engineering, Southeast University, Nanjing, China. [2]Wenzhou Institute, University of Chinese Academy of Sciences, Wenzhou, China. e-mail: yjzhao@njglyy.com

https://doi.org/10.1038/s41893-026-01872-1

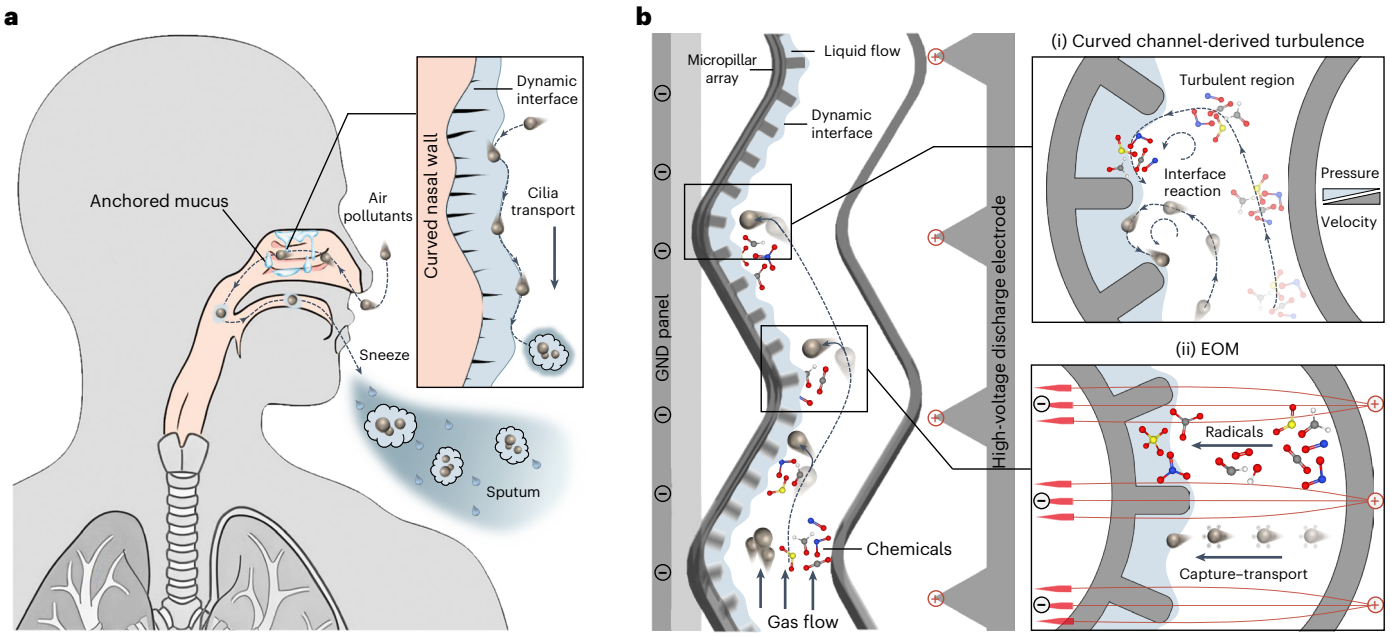


Fig. 1 | Schematic diagram of respiratory-inspired EOM for air purification. a, The mechanism of particle filtration function based on dynamic gas–liquid interface in the upper respiratory tract. **b**, The working principle of EOM, featured with dynamical gas–liquid interface, curved herringbone channel and high-voltage electrostatic field.

inspiration from such physiological function, our open-microfluidics was designed with a flexible hydrophilic micropillar array to anchor the functional liquid (FL) for forming the gas–liquid interface and with herringbone morphology open channels for fully exposing flowing air to the dynamic interface. Benefiting from the wettability of the FL, the PM in the air phase is preferentially absorbed at the gas–liquid interface. Additionally, as a high-voltage electrostatic field was integrated within the EOM system, abundant free radicals and electrons are generated to activate and polarize the PM and gas components (SO_2, NO_x, CO_2, volatile organic compounds and so on), which can promote their movement to the FL. Moreover, such an interface in the EOM can be kept stable and dynamically refreshed with the flowing FL and gas, with sufficient contact further improving the removal efficiency. Thus, the intelligent EOM system was demonstrated to have efficient air purification capacity as well as high anti-clogging and anti-corrosion properties. These features render the EOM system highly promising for effective PM removal and diverse air purification scenarios.

Results

Dynamic anchor of FL

In a typical experiment, the polydimethylsiloxane (PDMS) micropillar array was fabricated by replication of a 3D-printed template. Then, non-wetted hydrophobic PDMS was spray-coated with a hydrophilic layer for FL transport and dynamic anchor, composed of polyvinyl alcohol/silicone dioxide (PVA/SiO_2) after volatilization of ethanol (Fig. 2a and Supplementary Fig. 1). Scanning electron microscopy (SEM) and atomic force microscopy (AFM) images demonstrated that the surface roughness was enhanced with better hydrophilicity after modification of SiO_2 (Fig. 2b, Supplementary Fig. 2 and Supplementary Video 1). The hydrophilicity showed greater stability over a 7-day period compared with conventional O_2-plasma treatment (Supplementary Figs. 3 and 4). Such wettability differences led to corresponding behaviours (non-wetted and infiltration state) of FL droplet on different substrates (Supplementary Figs. 5 and 6 and Supplementary Video 2). As shown in Fig. 2c, FL could be transported due to liquid infiltration under anti-gravity condition, where the micropillar efficiently anchored the gas–liquid interface by both intermittent and continuous liquid supply (Supplementary Fig. 7 and Supplementary Video 3).

To elucidate the role of the gas–liquid interface, the correlations between interface height (h_i) and micropillar array parameters (height, h, and distance, d) were studied (Fig. 2d). According to Laplace's equation, the pressure and gravity of a curved liquid surface should meet the equilibrium, thus h_i could be defined as the following semi-empirical equation (details are included in Supplementary Note 1):

$$h_i = \alpha\left[h - \frac{2\gamma\cos\beta}{\rho g(d-d_p)}\right], \quad (1)$$

Where γ is surface tension, ρ is density, g is gravity, β is contact angle, d_p is micropillar diameter and α is an empirical coefficient related to FL flow rate. Through experiments, h_i showed a positive correlation with h and a negative correlation with d, in agreement with equation (1), as shown in Supplementary Fig. 8. For interfaces constructed with different liquids, the surface tension and contact angle played a critical role. The h_i of four types of FL were measured to be consistent with the above formula (Supplementary Fig. 9). As to α, it was observed that optimizing flow rates led to three primary flow patterns: liquid lining (<0.3 ml h^{-1}), dynamic anchoring and leakage (>20 ml h^{-1}) (Fig. 2e). The region between the lining and leakage regime was defined as the efficient regime, where the balance between fluidic inertial force and surface tension could be maintained.

Subsequently, the FL behaviours on curved micropillar array were investigated. The elastic modulus of the micropillar array showed a positive correlation with the weight ratio of the curing agent and substrate thickness (Supplementary Figs. 10 and 11). To balance mechanical strength and tensile capacity, a ratio of 15:1 and thickness of 1.5 mm were adopted for subsequent experiments, and the elastic modulus was found to maintain stablility under higher temperatures (40 °C and 60 °C), indicating stable mechanical strength in warm conditions (Supplementary Fig. 12). The finite element analysis of stress was performed, and the micropillars could effectively resist deformation under the condition of negative and positive curvatures (Fig. 2f,g). Then, the

https://doi.org/10.1038/s41893-026-01872-1

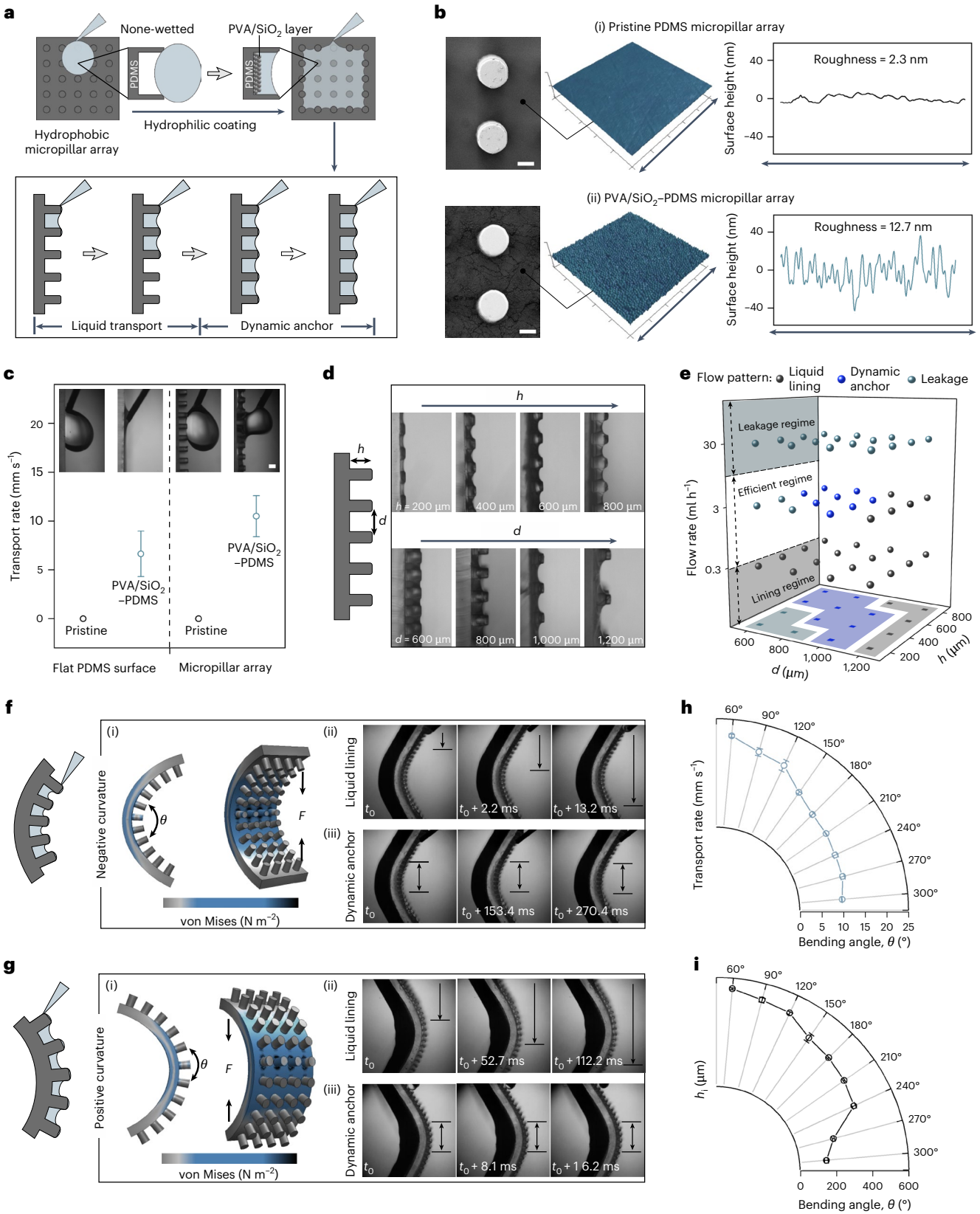


Fig. 2 | Dynamic gas–liquid interface anchored by micropillar array. a, Scheme of hydrophilic coating for dynamic anchor and liquid transport. **b**, SEM and AFM images of surface roughness of (i) pristine and (ii) PVA/SiO_2-modified PDMS. **c**, Plot of liquid transport rate on flat surface and micropillar array. **d**, Optical microscopy images of dynamic gas–liquid interface anchored by micropillar arrays with different ***d*** and ***h***. **e**, State diagram of liquid flow patterns as functions of ***d***, ***h*** and flow rate. **f**,**g**, Characterization of liquid flow pattern on micropillar array with negative (**f**) and positive (**g**) curvatures. (i) Finite element analysis of stress during bending. Optical microscopy images of (ii) liquid lining and (iii) dynamic anchor. **h**, Plot of transport rate as a function of increasing bending angle. **i**, Plot of h_i as a function of increasing bending angle. More than three independent images were captured, and all images showed similar results for **d**, **f** and **g**. Data are presented as mean ± s.d. of $n = 3$ independent measurements in **c**, **h** and **i**. Scale bars, 200 μm (**b**), 400 μm (**c**).

optical image sequences of liquid transport on curved micropillar arrays were recorded, revealing the ability to maintain the interface where the risk of fracture was also maintained when bending angle θ was smaller than 60° or larger than 300° (Supplementary Figs. 13 and 14). It was found that negative curvature surface possessed lower interface energy and solid–liquid contact area. Thus, the transport rate could be promoted by decreasing θ (Fig. 2h). Due to the bending-derived stretching of the region (increased d) between neighbouring micropillars, h_i decreased to a minimal value of around 140 µm (Fig. 2i), which was consistent with equation (1).

Particles and chemicals capture at dynamic gas–liquid interface

Given the stability of gas–liquid interfaces, and their capacity for dynamically refreshing, we applied such interfaces to capture and transport particles from the gas phase. As reported previously, most solid particles could easily adhere to the gas–liquid interface due to the change of surface free energy[35,36]. The primary forces at the interface included gravitational force, buoyancy force and surface tension force (Fig. 3a). The gravitational force and buoyancy force, in particular, were ignored because they were negligible compared to surface tension force. In most cases, the contact angle of particles is less than 180°, and the adhesion to interface can spontaneously occur where the surface free energy is strong enough to overcome the detachment energy. Whether the gas–liquid interface can further enter the FL once the particles adhere depends on its wettability. To validate this, the particles were subjected to contacting the air–FL interface, with the results confirming the moving process of the particles across the interface (Fig. 3b and Supplementary Video 4). Furthermore, the interactions between different particles (for example, sulfur powder, cigarette, wormwood and polystyrene) and FLs (for example, water, PVA, sodium dodecyl sulfate (SDS) and fluorinated oil-40 (FC-40)) were examined to explore the universality of the findings (Fig. 3c). It was observed that the capture ability presented a negative correlation with surface tension (Supplementary Fig. 15).

The real-time images of particle capture at dynamic gas–liquid interface were recorded by high-speed camera, where the particles in gas phase were obviously captured by the interface and subsequently transported along the FL flowing direction (Fig. 3d and Supplementary Video 5). It was found that the particle transport speed increased with increasing flow rate within the efficient regime (1 ml h^{-1}–20 ml h^{-1}), resulting in avoidance of liquid lining and leakage (Fig. 3e). After contact, the FL showed the Tyndall effect, and the dynamic light scattering demonstrated the efficient capture (Supplementary Fig. 16). These captured particles could be removed by high-speed centrifugation (10,000g, 20 min) for FL regeneration (Supplementary Fig. 17). As an alternative strategy, highly-efficient adsorbents (for example, activated carbon, mesoporous molecular sieves, metal organic frameworks and porous oxides) or catalysts (for example, transition metal oxide catalysts and photocatalytic systems) could be integrated with the FL chamber for further enrichment or industrial purification. The particle image velocimetry was also applied to analyse the time series images (Fig. 3f). The shear rate was obviously increased at the region surrounding the particle, revealing the efficient transport along the FL flow direction (Fig. 3g).

Aside from solid PMs, the gas chemicals, such as sulfur dioxide (SO_2), nitrogen oxides (NO_x), carbon dioxide (CO_2) and formaldehyde, could also be captured at the dynamic gas–liquid interface. By adding extra functional components, the gas chemicals could anchor at the interface and react with the FL. The vapour stream was flowing in the counter direction of the continuous gas flow (240 ml min^{-1}–500 ml min^{-1}) to avoid insufficient reaction and gas leakage. Specifically, sodium hydroxide (NaOH) and phenothalin served as the FL for capture and colourimetric sensing of acidic gas (SO_2, NO_x), where the hydrolysis ionization process caused protonation of phenothalin with obvious colour variations (Fig. 3h). Similarly, bromothymol blue (BTB) served as the FL for CO_2 with obvious colour changes due to analogical protonation and deprotonation (Fig. 3i). As for formaldehyde, 4-amino-5-hydrazino-1,2,4-triazole-3-thiol (AHMT) and potassium periodate (KIO_4) served as the FL. The intermediate product presented a change from colourless to purple after reaction with KIO_4 (Fig. 3j). In brief, the detailed components of the FL could be flexibly optimized according to the characteristic reaction of target gas chemicals.

Construction of EOM functional unit for air purification

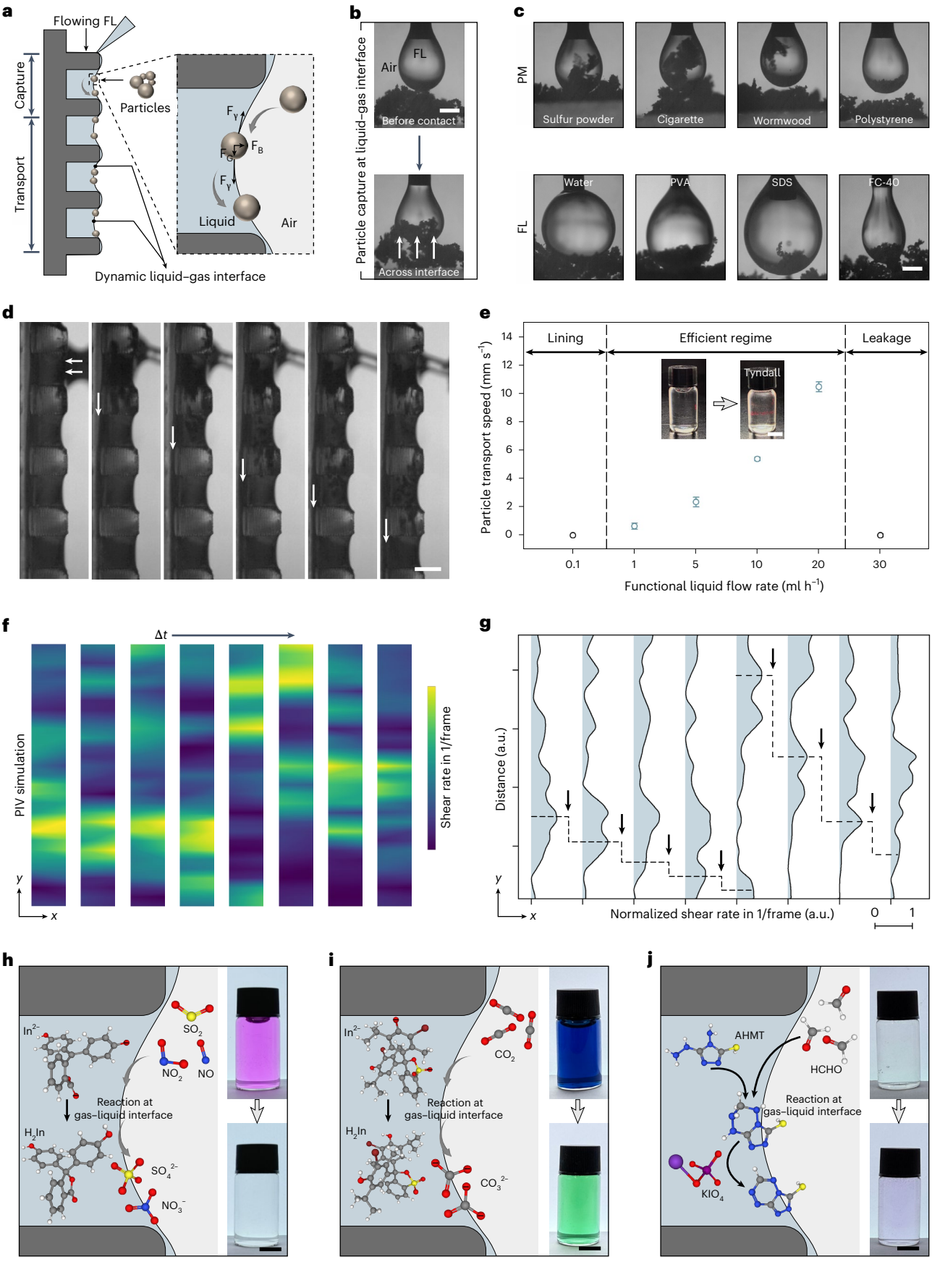
To improve the capture efficiency of gas–liquid interface, a high-voltage electrostatic field was integrated with open-microfluidics. The electrostatic field between a ground (GND) panel and thorn line caused air ionization and generated abundant positive ions or electricity, which were easily absorbed by neutral pristine particles (Fig. 4a). Due to the electrostatic attraction, the motion trajectories of particles were deflected to the GND panel, further enhancing the contact with interface. The electrostatic field also generated abundant free radicals (for example, hydroxyl radicals and oxygen radicals), which contributed to the polarization of chemicals for easier reaction with the interface.

To explore the underlying mechanism, we calculated the molecular structure and density distribution of several gas components (SO_2, NO_x, CO_2 and formaldehyde) in electrostatic field by density functional theory (Supplementary Fig. 18). The covalent bonds of gas molecules were stretched along the field direction and electrostatic potential was notably enhanced. The bond length increased as a function of electrical-field intensity, while Mayer and Laplacian bond order both followed a decreasing trend. These results demonstrated the activated state of polarized gas components for effective positive electricity adsorption. Thus, these gas molecules showed positive electricity and migrated towards the GND panel due to electric field attraction. The gas molecular structures under different temperatures (298 K, 333 K and 1,000 K) were also calculated with no differences, which indicated that the influence of thermal motion was negligible compared with electrical field (Supplementary Fig. 19). Subsequently, several electrostatic field parameters were numerically simulated, including electrical potential, electric-field intensity and space-charge density featured with stable intensity and charge distribution (Fig. 4b and Supplementary Fig. 20, details are included in Supplementary Note 2). The smoke gas flow pumped from the bottom of the electrostatic field was observed with a distinct deflection (Fig. 4c(i) and Supplementary Video 6). The deflection distance showed a negative correlation with voltage and electric field force (Supplementary Fig. 21), but increased as a function of panel spacing (Supplementary Fig. 22). However, panel spacing that was too narrow caused electric breakdown and impacted the operation safety.

The motion trajectories of particles with different sizes were simulated in Fig. 4c(ii). We found that larger particles were easier to

Fig. 3 | Capture of particles and chemicals at dynamic gas–liquid interface. **a**, Scheme of gas–liquid interface to capture and transport the particles from the gas phase. F_B is the buoyance force, F_G is the gravity, and F_γ is the surface tension. **b**, Optical microscopy images of particle capture process at gas–liquid interface. **c**, Optical microscopy images of different kinds of particles captured by different FLs. **d**, Optical microscopy images of the capture and transport of particles from the gas phase. **e**, Plot of particle transport speed as function of FL flow rate. The inner photograph shows the Tyndall effect of FL after particle capture. **f**, Time series images of particle image velocimetry (PIV) simulation contours. **g**, The normalized shear rates distribution along the FL flow direction. **h**–**j**, Scheme and photographs of capture and colourimetric sensing of target chemicals: SO_2, NO, NO_2 by NaOH/phenothalin (**h**); CO_2 by BTB (**i**); and formaldehyde by AHMT/KIO_4 (**j**). More than three independent images were captured, and all images showed similar results for **b**, **c** and **d**. Data are presented as mean ± s.d. of $n = 3$ independent measurements in **e**. Scale bars, 1 mm (**b**,**c**), 400 µm (**d**), 7 mm (**e**), 8 mm (**h**,**i**,**j**).

https://doi.org/10.1038/s41893-026-01872-1



https://doi.org/10.1038/s41893-026-01872-1

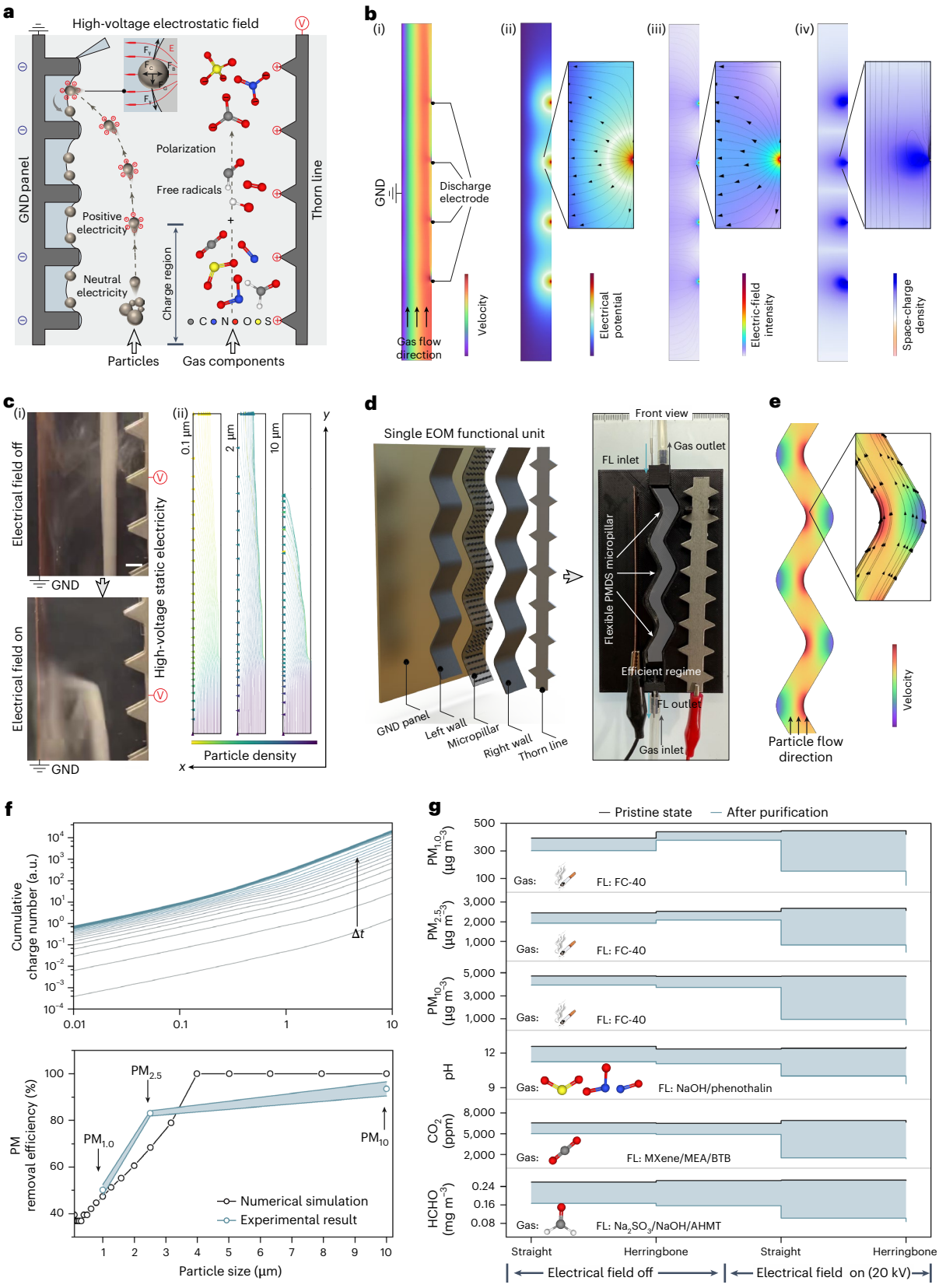


Fig. 4 | Construction of EOM functional unit for air purification. a, Scheme of high-voltage electrostatic field integrated with open-microfluidics for the capture of particles and chemicals. **b**, Numerical simulations of (i) gas flow velocity, (ii) electrical potential, (iii) electric-field intensity and (iv) space-charge density in the electrostatic field. **c**, Characterization of gas deflection in electrostatic field. (i) Photographs of gas flow under the electric field with off/on state. (ii) Numerical simulations of motion trajectories of particles with different sizes. **d**, Scheme and photograph of a single EOM functional unit. **e**, The velocity contour of the gas flow within herringbone channel. **f**, Plot of cumulative charge number and removal efficiency as a function of the particle size. **g**, Purification of different components in polluted air by optimized EOM system with respective FLs. Scale bar, 6 mm.

deflect towards the GND panel due to stronger electricity adsorption. In brief, the purification efficiency, η, can be defined as following a semi-empirical equation (details are included in Supplementary Note 3)

$$\eta = 1 - e^{-\frac{\varepsilon_0 \varepsilon_{RH}}{\varepsilon_{RH}+2} \times \frac{A d_{PM} (E_0 \kappa_{RH})^2}{Q\mu(T)}},$$
$$\begin{cases} \mu(T) = \mu_0 \left(\frac{T}{T_0}\right)^{1.5} \frac{T_0 + S_T}{T + S_T} \\ A = 2n\pi \frac{\sqrt{2}d - d_p}{d - d_p} \times \frac{1}{\rho g \tan\beta} \end{cases} \quad (2)$$

where ε_{RH} is dimensionless relative dielectric constant of particles regarding environmental humidity, ε_0 is the vacuum dielectric constant, A is the area of gas–liquid interface (n is number of repeated four square-arranged micropillars, β is equal to static contact angle), d_{PM} is particle diameter, E_0 is electric field intensity, κ_{RH} is humidity correction coefficient, $\mu(T)$ is gas viscosity related with environmental temperature, T is practical temperature, T_0 is 273 K, S_T is sutherland coefficient of gas flow and Q is gas flow rate. Thus, by increasing E_0, the purification efficiencies of PMs ($PM_{1.0}$, $PM_{2.5}$, PM_{10}) were substantially improved, which was consistent with equation (2) (Supplementary Fig. 23). Increasing electrode distance would lead to a dead zone between neighbouring electrodes, which featured low electric-field intensity and space-charge density (Supplementary Fig. 24). However, too small a distance inevitably induced electric breakdown phenomenon and impacted the field stability. Based on simulation and experimental results, the final electrode distance was set as 1.5 cm for subsequent experiments. The curved dynamic gas–liquid interface before the GND panel notably increased A and improved purification efficiency, and the flexible hydrophilic micropillar array could easily be fabricated with larger A according to the practical requirements of large-space applications for high-concentration pollutants. Thus, the herringbone channel was selected to replace the straight channel and generate geometry-derived turbulence. The single EOM functional unit contained a GND panel, left/right herringbone wall, flexible micropillar array and a thorn line. Benefitting from lego-microfluidics-inspired design, single units could be spliced with each other to constitute an integral EOM system (Fig. 4d and Supplementary Fig. 25). The velocity contour in the herringbone channel was simulated in Fig. 4e, revealing disturbed velocity and pressure distribution near the curved region (Supplementary Figs. 26 and 27). The characteristic angle (θ_h) was optimized at 120° to induce efficient gas turbulence and avoid gas retention (Supplementary Fig. 28), and the curved geometric channel showed quick purification of smoke air (Supplementary Fig. 29). Subsequently, the cumulative charge number of particles with different sizes was simulated, revealing that larger particles showed more positive electricity after entering the electrostatic field (Fig. 4f and Supplementary Note 3). The specific removal efficiency of PMs was detected (83.30% for $PM_{1.0}$, 89.72% for $PM_{2.5}$ and 94.33% for PM_{10}) using herringbone channel rather than straight channel (Supplementary Fig. 30).

Additionally, the components of FL were flexibly selected according to respective targets. For example, FC-40 served as the FL for PMs; NaOH/phenothalin served to absorb SO_2 and NO_x; MXene/monoethanolamine (MEA)/BTB served to absorb CO_2; and NaOH/sodium sulfite (Na_2SO_3)/AHMT was used to absorb formaldehyde. The corresponding concentration or sensing index were detected in Fig. 4g. Overall, the air purification capacity of the EOM system was based on the integration of open-microfluidics with high-voltage electrostatic field. The practical purification of different components (PMs, SO_2, NO_x, CO_2 and formaldehyde) in polluted air was examined under different voltages (Supplementary Table 1).

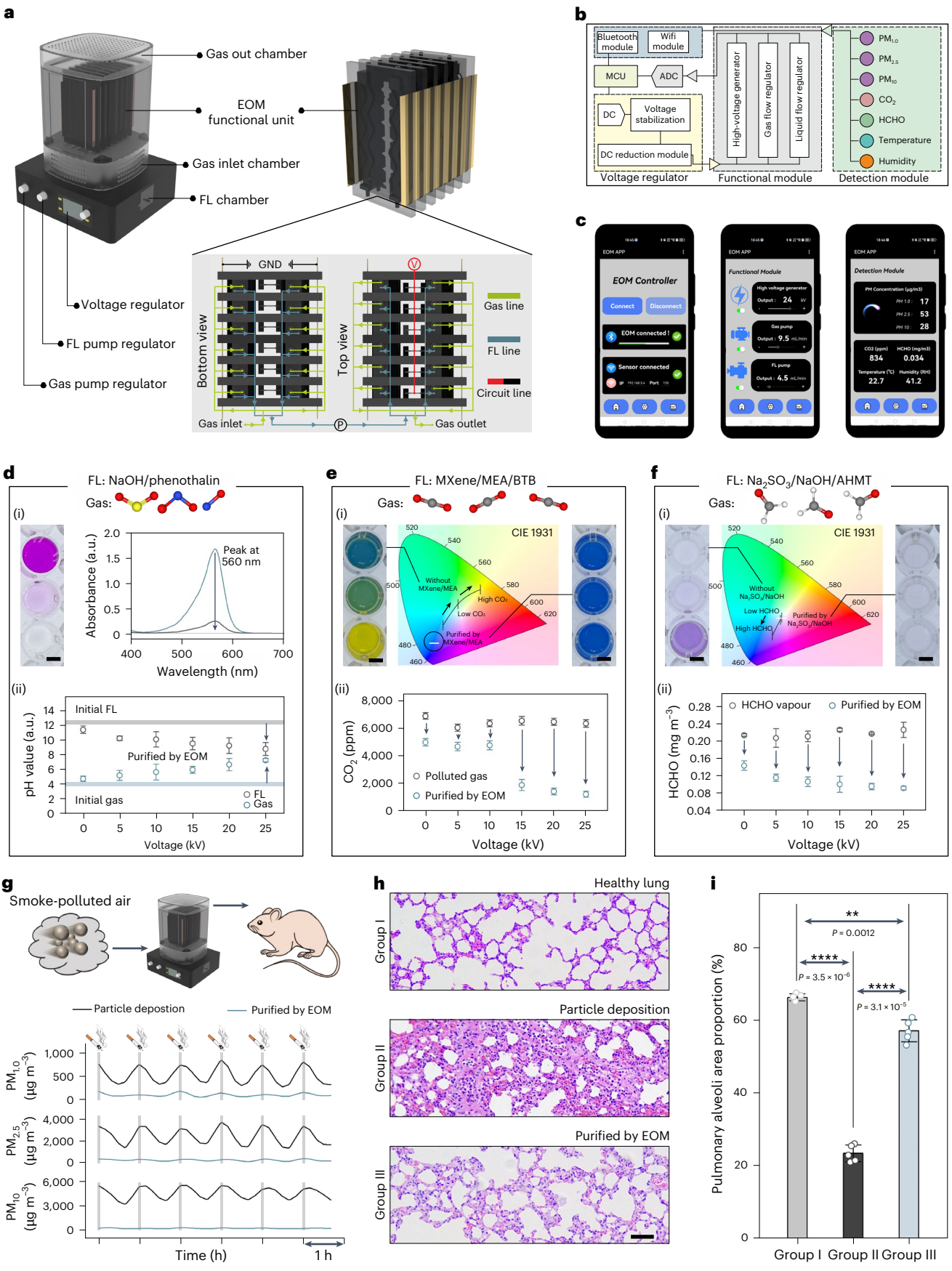
Extended applications of an EOM device for different scenarios

To broaden the potential applications, we constructed an integral EOM device (Fig. 5a and Supplementary Fig. 31). In detail, the EOM device contained a high-voltage generation module, multiple EOM functional units and a pump module. The high-voltage electrostatic field was generated by a transformer with adjustable inputs. The pump module contained two separated pumps for gas and FL. The FL and gas pipelines were connected with multiple EOM functional units and a FL chamber for controllable supply (Supplementary Fig. 32). Such hierarchical air inflow channels and dynamically regulated valves, along with regulated flow rates and intake volumes, could efficiently reduce the burden of extreme polluted applications. Also, wireless manipulation was developed between the device and a customized mobile phone application for intelligent operation (Fig. 5b and Supplementary Fig. 33). The high-voltage generator and gas/liquid flow regulator could be precisely adjusted by microprocessor via bluetooth communication. In addition, the real-time monitoring of several indexes ($PM_{1.0}$, $PM_{2.5}$, PM_{10}, CO_2, formaldehyde, temperature and humidity) was achieved by wireless fidelity communication with commercial sensors, whose data was transmitted to the mobile application interface (Fig. 5c).

The experimental system for air purification and detection was self-constructed, with the pressure being real-time regulated around 101 kPa and the surrounding temperature was maintained around 20 °C (Supplementary Fig. 34). In our work, the visual detection of gaseous components was realized by recording respective RGB colour variations. By converting to chromatic co-ordinates in CIE diagrams, the concentration variations could be visually detected. For specific gaseous components, different indicator systems bearing obvious RGB colour changes were adopted. For industrial acidic gases (plenty of SO_2 and NO_x), phenothalin was added into NaOH (1 mol l^{-1}) solution as the FL, which turned from purple to colourless with decreased intensity of characteristic peak (560 nm) due to the acid–base neutralization reaction (Fig. 5d). The change of chrominance co-ordinate was recorded as colourimetric sensing index (Supplementary Fig. 35). By integrating BTB as an indicator, MXene (0.1 wt%) was added into MEA solution as the FL for CO_2 (Fig. 5e). The protonation of BTB induced by CO_2 was hindered by a CO_2–MEA reaction, where MXene enhanced carbon affinity for absorption (Supplementary Fig. 36). The chrominance co-ordinate was recorded for colourimetric detection of CO_2, which revealed that the electrostatic field-derived polarization was efficient to improve purification efficiency. For formaldehyde, Na_2SO_3 (1 mol l^{-1}) was added into NaOH solution as absorbent and AHMT/KIO_4 served as the indicator (Fig. 5f). The formaldehyde-specific chromogenic reaction was hindered by Na_2SO_3 in alkaline environments, and the FL maintained colourless. The decrease of characteristic peak (550 nm) intensity confirmed the adsorption of formaldehyde evaporation (Supplementary Fig. 37).

Fig. 5 | Extended applications of EOM system. a, Scheme of integral EOM-based device. **b**, System-level block diagram of the device. **c**, Custom mobile application for wireless operation and data acquisition. DC, direct current power supply. **d**, Purification and detection of acidic gases. (i) Photograph and respective UV-visible spectrum of FL before and after purification. (ii) Plot of the pH value of the gas and FL as a function of voltage. **e**, Purification and detection of CO_2. (i) Photograph and CIE chromaticity diagram co-ordinates of FL under the conditions of CO_2 with different concentrations. (ii) Plot of CO_2 concentration as a function of voltage. **f**, Purification and detection of formaldehyde. (i) Photograph and CIE chromaticity diagram co-ordinates of FL under the conditions of formaldehyde with different concentrations. (ii) Plot of formaldehyde concentration as a function of voltage. **g**, Real-time concentrations of PMs during the animal experiment. **h**, H&E-stained images of pulmonary alveoli of three groups. **i**, Plot of pulmonary alveoli area proportion of three groups. Data are presented as mean ± s.d. of $n = 5$ independent measurements in **d**, **e**, **f** and **i**. Scale bars, 0.5 cm (**d**,**e**,**f**), 50 μm (**h**). P values are determined by ordinary one-way analysis of variance. $^{**}P < 0.01$, $^{****}P < 0.0001$. ADC, analogue to digital converter; MCU, microcontroller unit.

https://doi.org/10.1038/s41893-026-01872-1



Moreover, the Gibbs free energy changes of reactions between gas components and free radicals were calculated with spontaneous tendency (Supplementary Table 2). To achieve synergistic removal of multiple components, we expanded two assembly models (in series and in parallel) of EOM functional units. For the in-series model, two single units were circulated individually with different FLs (FC-40 for the first unit and a water-based FL for the second unit). For the in-parallel model, SDS served as the FL, with several water-based liquids added for the gas components capture. It was demonstrated that different targets could be synergistically purified with high efficiency (Supplementary Fig. 38). The amplification of functional units was feasible based on in-series or in-parallel connections to satisfy the requirements of large gas volume and pollutants concentration in practical industrial applications.

The stability and safety of the EOM device for long-term operations were subsequently examined. During a 72-h working period, the concentration of generated ozone was monitored to be within the safe concentration range, and electrical breakdown phenomenon was not observed (Supplementary Fig. 39). The timely transport of particles by the dynamic interface endowed the EOM device with anti-pollution property, where no residual pollutants were observed on the substrate after 72 h (Supplementary Fig. 40). The anti-corrosion property was also characterized under different acidic or alkaline environments for 7 days, including sodium hydroxide (NaOH, 1 mol l^{-1}), sodium chloride (NaCl, 1 mol l^{-1}) and sulfuric acid (H_2SO_4, 0.5 mol l^{-1}). It was found that the surface was not obviously etched and maintained stable hydrophilicity (Supplementary Fig. 41). The diameter and height of micropillars were also measured with no obvious variations in different working solutions (Supplementary Fig. 42). Then, the purification performance of the EOM device in a larger space (1 m length × 1 m width × 1 m height) was tested, where the polluted air could be purified to safe levels within 2 h (Supplementary Fig. 43). We explored the influence of air flow rates on purification efficiency (Supplementary Table 3). To resist the gas shear force derived from high-speed airflow, the micropillar height was increased with decreased distance to enhance the spatial confinement effect and contact-specific surface area (Supplementary Fig. 44). The clean air volume appeared to be positively correlated with air flow rate (0–1,000 ml min^{-1}) due to the low gas resistance of open-microfluidics. These experimental results demonstrated that the EOM system could maintain a stable state under complex industrial conditions with long working lifespan.

The EOM device was also applied to protect the lungs of mice from excessive particle inhalation. The healthy mice were classified into three groups: group I (fresh air), group II (smoke-polluted air) and group III (EOM-purified smoke). The experimental period for each group was 10 days, with gas supplied at 1-h intervals. The PM concentrations were real-time detected and hematoxylin-eosin (H&E) staining was performed to better evaluate the degree of lung injury (Fig. 5g,h). Compared with group I, the pulmonary alveoli of group II were obviously atrophied due to excessive particle deposition. In contrast, group III maintained a healthy state similar to group I. The pulmonary alveoli area proportion was calculated, which implied that most PMs were purified with minimized lung damage (Fig. 5i). These results demonstrate the potential of EOM-based devices for different practical scenarios, having low economic cost and low pressure drop, great sustainability, system integration capabilities and efficiency of purification (Supplementary Fig. 45).

Discussion

In conclusion, an EOM device was reported for respiratory-inspired air purification. Compared with traditional air purification strategies, our EOM system showed priority on the great sustainability benefiting from the dynamically refreshed gas–liquid interface. The flowing FL not only transported the particles and chemicals along the direction of flow with high efficiency, but also prevented corrosion and excessive deposition, and demonstrated low cost and prolonged service life. Additionally, the capture mechanism based on wettability at the gas–liquid interface could be expanded to broader targets, including PMs, aerosols, gas chemicals (SO_2, NO_x, CO_2, volatile organic compounds and so on) and even some pathogens. Moreover, the components of FLs could be flexibly optimized for efficient adsorption and colourimetric sensing of specific targets at different application scenarios. Overall, these features render the EOM system highly promising for effective PM removal and diverse air purification scenarios. Future studies should focus on enhancing the stability and system scalability of EOMs for domestic and commercial use, as well as looking at other arrangement patterns of the micropillar array and channels to improve purification performance.

Methods

Materials

SiO_2 nanoparticles with a diameter of 216 nm were self-synthesized according to the typical Stöber method. PDMS (SYLGARD 184) was obtained from Dow Corning. NaOH, Na_2SO_3, ethanol, phenothalin, BTB, formaldehyde, dry ice and MEA were obtained from Nanjing Wanqing Chemical Glassware & Instrument. Mxene solution was bought from Nanjing XFNano Materials Tech Co., Ltd. The 3M Fluorinert FC-40 was acquired from 3M Co., Ltd. PVA was purchased from Sigma-Aldrich. SDS, AHMT and KIO_4 were bought from Shanghai Macklin Biochemical Co., Ltd. Distilled water used in all experiments was purified by a Milli-Q Plus 185 water purification system (Millipore) with a resistivity higher than 18 MΩ cm.

Fabrication of hydrophilic PVA/SiO_2-modified PDMS micropillar array

First, the moulds of the micropillar array bearing different heights and distances were fabricated by three-dimensional (3D) digital light project printing technology (NanoArch). The moulds were immersed in the ethanol and subjected to 24 h ultraviolet light irradiation to remove the uncured polyethylene glycol diacrylate resin. The PDMS precursor was mixed with curing agent bearing different weight ratios (1:10, 1:12.5, 1:15, 1:17.5 and 1:20) and poured onto the moulds with a pre-designed thickness. After removing the air from the solution in a vacuum environment, PDMS was totally cured at 80 °C for 2 h. The PDMS surface was pre-treated by O_2 plasma for 30 s. Then, 5 ml PVA solution (2 wt%) was mixed with 5 ml SiO_2/ethanol solution (20 wt%) as the coating solution after sonication for 30 min at 10 °C. Then, the rotational speed of spray coating was set as 1,000 rpm for 30 s. Afterwards, the PDMS micropillar array was transferred to a hot plate set at 90 °C for 5 mins to evaporate the ethanol and yield the long-term hydrophilic layer. The surface roughness was characterized by a field scanning electron microscope (Ultra Plus, Zeiss) and an atomic force microscope (Dimension, ICON). The optical microscopy images were recorded by a stereoscopic microscope (Jiang Nan) equipped with a CCD camera (Olympus, DP30BW). The real-time images of liquid transport were recorded by a microscope (Olympus, CKX53) equipped with a high-speed camera (S-PRI F1, AOS Technologies AG).

Characterization of the elastic property of PDMS substrates

The PDMS micropillar arrays, with different curing agent ratios (1:10, 1:12.5, 1:15, 1:17.5 and 1:20) and different thicknesses (0.5, 1, 1.5 and 2 mm), were cut into the patch with rectangle shape. Then, the patch was fixed on the tensile machine (ASTM, F2258) at the initial unstretched state, which then programmatically moved at a constant speed of 1 mm min^{-1}. The real-time force and displacement data were recorded. The fracture energy was calculated by integration of the stress–strain plot, which indicated the rigidity property. The elastic modulus was obtained by calculating the initial slope of the stress–strain plot, which indicated the elastic property.

Capture and sensing of the chemicals at the gas–liquid interface

The FLs were flexibly selected according to the characteristic reactions with different target chemicals. For industrial acidic effluents (SO_2, NO and NO_2), NaOH/phenothalin was selected as the FL. The primary reactions contained $SO_2 + \cdot O + H_2O \rightarrow H_2SO_4$ and $NO_X + \cdot O/\cdot OH + H_2O \rightarrow HNO_3$. The generated acidic products would react with NaOH and lead to protonation of phenothalin. For CO_2, Mxene/MEA/BTB was selected as the FL. The primary reaction was $CO_2 + 2RNH_2 \rightarrow RNH_3^+ + RNHCOO^-$, where MXene served as the auxiliary reagents to absorb more CO_2. Such reaction hindered the combination of CO_2 and BTB, prevented the protonation of phenothalin and meant that the FLs maintained their blue colour. For formaldehyde, Na_2SO_3/NaOH/AHMT was selected as the FL. The primary reaction was $HCHO + Na_2SO_3 + H_2O \rightarrow HOCH_2SO_3Na + NaOH$. The high-voltage electrostatic field contributed to the reactions between formaldehyde and abundant free radicals (for example, $HCHO + \cdot O/\cdot OH \rightarrow \cdot CHO/HCOOH \rightarrow CO_2 + H_2O$). These reactions hindered the chromogenic reaction between the formaldehyde and AHMT/KIO_4 and meant that the FL remained colourless.

Fabrication of the EOM-based device

The components of the integral device were fabricated based on fused deposition 3D printing technology (Bambu Lab, P1S). The accurate geometric structures and respective engineering drawings were established by SOLIDWORKS and AutoCAD software. Then, several kinds of printing materials were used to construct the device framework, including acrylonitrile butadiene styrene plastic and transparent polyethylene terephthalate-I. The connections of the different chambers were based on the pre-designed threaded screw. The pipelines for the transport of gas and FL were realized by polyethylene tubes with different inner diameters. The high-voltage electrostatic field (0–30 kV) was generated from a transformer with adjustable inputs (0–24 V), whose output terminals were connected with ground panel and thorn lines, respectively. The printed circuit board was self-prepared with pre-designed functions as the controller of the EOM-based device, including the bluetooth communication, output voltage regulation and voltage stabilization. Additionally, the commercial gas sensors were integrated with this device through wireless communications to transport the real-time sensing data.

Animal experiments

Adult (8–12-week-old) Sprague-Dawley rats originally obtained from Charles River were housed and bred in the animal facility at Southeast University. The animal room was maintained in an environment with a humidity of 40–60% and a temperature of 18–23 °C under a 12 h light/12 h dark cycle. The rats were used as the lung donors for experiments. All animals were handled strictly according to the recommendations in the 'Guide for the Care and Use of Laboratory Animals'. All animal care and experimental protocols were reviewed and approved by the Animal Experimental Ethics Inspection of Southeast University (20240926002). Healthy mice were randomly divided into three groups (5 mice per group), including a control group (fresh air) and two experimental groups (untreated smoke air and EOM-purified smoke). For the two experimental groups, the smoke for each was generated by burning cigarettes with smoked wood, and it was then transferred to the sealed box that was equipped with three-way valves. The breathing interval was set as 1 h to avoid unpredictable death due to suffocation during the 10-day period. Afterwards, the lungs of the mice in the three groups were dissected to identify the damage caused by excessive particle depositions. Finally, the lung samples were dehydrated, embedded in paraffin and sliced for further H&E staining. The pulmonary alveoli area proportion was calculated by Image J software.

Reporting summary

Further information on research design is available in the Nature Portfolio Reporting Summary linked to this article.

Data availability

All data are presented in the article and its Supplementary Information. Source data are provided with this paper.

Code availability

Codes used in this study for custom mobile application are available at https://osf.io/gzw8h.

References

1. Zhao, Y. H. et al. Air pollution modulates trends and variability of the global methane budget. *Nature* **642**, 369–375 (2025).
2. Huang, W. et al. Toward cleaner air and better health: current state, challenges, and priorities. *Science* **385**, 386–390 (2024).
3. Ji, J. S., Dominici, F., Gouveia, N., Kelly, F. J. & Neira, M. Air pollution interventions for health. *Nat. Med.* **31**, 2888–2900 (2025).
4. Apte, J. S. & Manchanda, C. High-resolution urban air pollution mapping. *Science* **385**, 380–385 (2024).
5. Hill, W. et al. Lung adenocarcinoma promotion by air pollutants. *Nature* **616**, 159–167 (2023).
6. Freese, L. M., Chossière, G. P., Eastham, S. D., Jenn, A. & Selin, N. E. Nuclear power generation phase-outs redistribute US air quality and climate-related mortality risk. *Nat. Energy* **8**, 492–503 (2023).
7. Thurston, G. D., Chen, L. C. & Campen, M. Particle toxicity's role in air pollution. *Science* **375**, 506–507 (2022).
8. Gu, B. J. et al. Abating ammonia is more cost-effective than nitrogen oxides for mitigating PM2.5 air pollution. *Science* **374**, 758–762 (2021).
9. Liang, B. et al. Microporous membranes comprising conjugated polymers with rigid backbones enable ultrafast organic-solvent nanofiltration. *Nat. Chem.* **10**, 961–967 (2018).
10. Jin, X. Y. et al. Direct air capture of CO_2 in an electrochemical hybrid flow cell with a spatially isolated phenazine electrode. *Nat. Energy* **10**, 1146–1154 (2025).
11. Li, Y. Y. et al. Semi-interpenetrating polymer network biomimetic structure enables superelastic and thermostable nanofibrous aerogels for cascade filtration of PM2.5. *Adv. Funct. Mater.* **30**, 1910426 (2020).
12. Kwon, H. J. et al. Long-lifetime water-washable ceramic catalyst filter for air purification. *Nat. Commun.* **14**, 520 (2023).
13. Zhang, G. H. et al. High-performance particulate matter including nanoscale particle removal by a self-powered air filter. *Nat. Commun.* **11**, 1653 (2020).
14. Wang, Q. F. et al. Polarity-dominated stable N97 respirators for airborne virus capture based on nanofibrous membranes. *Angew. Chem. Int. Ed.* **60**, 23756–23762 (2021).
15. Li, H. G. et al. Capturing carbon dioxide from air with charged-sorbents. *Nature* **630**, 654–659 (2024).
16. Wang, J. C. Nanofibrillated collagen fiber networks for enhanced air purification. *Nat. Commun.* **16**, 6823 (2025).
17. Wang, Y. H. et al. Nature-inspired micropatterns. *Nat. Rev. Methods Primers* **3**, 68 (2023).
18. Islamoglu, T. et al. Metal-organic frameworks against toxic chemicals. *Chem. Rev.* **120**, 8130–8160 (2020).
19. Qu, Z. Y. et al. Bubble wall confinement-driven molecular assembly toward sub-12 nm and beyond precision patterning. *Sci. Adv.* **9**, eadf3567 (2023).
20. Yang, C. Y., Yu, Y. R., Shang, L. R. & Zhao, Y. J. Flexible hemline-shaped microfibers for liquid transport. *Nat. Chem. Eng.* **1**, 87–96 (2024).
21. Zhou, M. J. et al. Ultralight electrospun composite filters with vertical ternary spatial network for high-performance $PM_{0.3}$ purification. *Adv. Mater.* **37**, 2419389 (2025).
22. Park, J. et al. Bioinspired capillary force-driven super-adhesive filter. *Nature* **643**, 388–394 (2025).

23. Shi, P. J. et al. Air plastron-enabled heat management for enhanced photothermal actuation in underwater soft robots. *Sci. Adv.* **1**, eadx7189 (2025).
24. Liu, M., Wang, S. & Jiang, L. Nature-inspired superwettability systems. *Nat. Rev. Mater.* **2**, 17036 (2017).
25. Yang, Z. Y. et al. CeyeHao: AI-driven microfluidic flow programming with hierarchically assembled obstacles and receptive field-augmented neural network. *Sci. Adv.* **1**, eadx7189 (2025).
26. Chen, C. et al. Bio-inspired multimodal soft actuator with environmental self-adaptation. *Nat. Commun.* **16**, 7630 (2025).
27. Hou, X., Hu, Y., Grinthal, A., Khan, M. & Aizenberg, J. Liquid-based gating mechanism with tunable multiphase selectivity and antifouling behaviour. *Nature* **519**, 70–73 (2015).
28. Sheng, Z. Z. et al. Liquid gating elastomeric porous system with dynamically controllable gas/liquid transport. *Sci. Adv.* **4**, eaao6724 (2018).
29. Jeong, S. et al. Human circulatory/respiratory-inspired comprehensive air purification system. *Adv. Mater.* **36**, 2405568 (2024).
30. Zhang, Y. M. et al. Continuous air purification by aqueous interface filtration and absorption. *Nature* **610**, 74–80 (2022).
31. Chen, H. X. et al. Biomimetic air purification with liquid-gating topological gradient microfluidics. *Nat. Chem. Eng.* **1**, 650–660 (2024).
32. Wang, C. C. et al. Airborne transmission of respiratory viruses. *Science* **373**, eabd9149 (2021).
33. Sznitman, J. Revisiting airflow and aerosol transport phenomena in the deep lungs with microfluidics. *Chem. Rev.* **122**, 7182–7204 (2022).
34. Man, W. H., Piters, W. A. A. D. & Bogaert, D. The microbiota of the respiratory tract: gatekeeper to respiratory health. *Nat. Rev. Microbiol.* **15**, 259–270 (2017).
35. Dinsmore, A. D. et al. Colloidosomes: selectively permeable capsules composed of colloidal particles. *Science* **298**, 1006–1009 (2002).
36. Binks, B. P. & Lumsdon, S. O. Influence of particle wettability on the type and stability of surfactant-free emulsions. *Langmuir* **16**, 8622–8631 (2000).

Acknowledgements

Funding: Y.Z. discloses support for the research of this work from the National Natural Science Foundation of China (T2225003), the Key Research & Development Program of Jiangsu Province (No.BE2023653), the Joint Fund of Henan Province Science and Technology R&D Program (NO.225200810021), the Clinical Trials from Nanjing Drum Tower Hospital (2022-LCYJ-ZD-01) and the research funding of Yangtze River Pharmaceutical Group. H.C. discloses support for the research of this work from the National Natural Science Foundation of China (224B2204) and SEU Innovation Capability Enhancement Plan for Doctoral Students (CXJH_SEU 25003). N.L., M.L. and J.W. declare no relevant funding.

Author contributions

Y.Z. supervised the project. Y.Z. and H.C. conceived the idea. H.C. performed experiments and data analysis. H.C. and Y.Z. wrote and revised the paper. H.C., N.L., M.L., J.W. and Y.Z. contributed to scientific discussion of the article.

Competing interests

The authors declare no competing interests.

Additional information

Supplementary information The online version contains supplementary material available at https://doi.org/10.1038/s41893-026-01872-1.

Correspondence and requests for materials should be addressed to Yuanjin Zhao.

Peer review information *Nature Sustainability* thanks John Chew, Taotao Fu and Xu Hou for their contribution to the peer review of this work. Peer reviewer reports are available.

Reprints and permissions information is available at www.nature.com/reprints.

Publisher's note Springer Nature remains neutral with regard to jurisdictional claims in published maps and institutional affiliations.

Springer Nature or its licensor (e.g. a society or other partner) holds exclusive rights to this article under a publishing agreement with the author(s) or other rightsholder(s); author self-archiving of the accepted manuscript version of this article is solely governed by the terms of such publishing agreement and applicable law.

© The Author(s), under exclusive licence to Springer Nature Limited 2026

nature portfolio

Corresponding author(s): Yuanjin Zhao

Last updated by author(s): May 6, 2026

Reporting Summary

Nature Portfolio wishes to improve the reproducibility of the work that we publish. This form provides structure for consistency and transparency in reporting. For further information on Nature Portfolio policies, see our Editorial Policies and the Editorial Policy Checklist.

Statistics

For all statistical analyses, confirm that the following items are present in the figure legend, table legend, main text, or Methods section.

n/a	Confirmed	
☐	☒	The exact sample size (*n*) for each experimental group/condition, given as a discrete number and unit of measurement
☐	☒	A statement on whether measurements were taken from distinct samples or whether the same sample was measured repeatedly
☐	☒	The statistical test(s) used AND whether they are one- or two-sided *Only common tests should be described solely by name; describe more complex techniques in the Methods section.*
☐	☒	A description of all covariates tested
☐	☒	A description of any assumptions or corrections, such as tests of normality and adjustment for multiple comparisons
☐	☒	A full description of the statistical parameters including central tendency (e.g. means) or other basic estimates (e.g. regression coefficient) AND variation (e.g. standard deviation) or associated estimates of uncertainty (e.g. confidence intervals)
☐	☒	For null hypothesis testing, the test statistic (e.g. *F*, *t*, *r*) with confidence intervals, effect sizes, degrees of freedom and *P* value noted *Give P values as exact values whenever suitable.*
☒	☐	For Bayesian analysis, information on the choice of priors and Markov chain Monte Carlo settings
☒	☐	For hierarchical and complex designs, identification of the appropriate level for tests and full reporting of outcomes
☒	☐	Estimates of effect sizes (e.g. Cohen's *d*, Pearson's *r*), indicating how they were calculated

Our web collection on statistics for biologists contains articles on many of the points above.

Software and code

Policy information about availability of computer code

Data collection	N/A
Data analysis	N/A

For manuscripts utilizing custom algorithms or software that are central to the research but not yet described in published literature, software must be made available to editors and reviewers. We strongly encourage code deposition in a community repository (e.g. GitHub). See the Nature Portfolio guidelines for submitting code & software for further information.

Data

Policy information about availability of data

All manuscripts must include a data availability statement. This statement should provide the following information, where applicable:

- Accession codes, unique identifiers, or web links for publicly available datasets
- A description of any restrictions on data availability
- For clinical datasets or third party data, please ensure that the statement adheres to our policy

All data are presented in the article and its Supplementary Information. Source data are provided with this paper

Research involving human participants, their data, or biological material

Policy information about studies with human participants or human data. See also policy information about sex, gender (identity/presentation), and sexual orientation and race, ethnicity and racism.

Reporting on sex and gender	N/A
Reporting on race, ethnicity, or other socially relevant groupings	N/A
Population characteristics	N/A
Recruitment	N/A
Ethics oversight	N/A

Note that full information on the approval of the study protocol must also be provided in the manuscript.

Field-specific reporting

Please select the one below that is the best fit for your research. If you are not sure, read the appropriate sections before making your selection.

☒ Life sciences ☐ Behavioural & social sciences ☐ Ecological, evolutionary & environmental sciences

For a reference copy of the document with all sections, see nature.com/documents/nr-reporting-summary-flat.pdf

Life sciences study design

All studies must disclose on these points even when the disclosure is negative.

Sample size	Animal numbers for each experiment are provided in the figure captions. Each quantitative experiment was performed in 5 replicates.
Data exclusions	Representative images were shown in the manuscripts; similar results from experimental repeats were not shown. No data excluded from statistical analyses.
Replication	All experimental were replicated for at least three times and performed independently
Randomization	All animals and biosamples were randomly allocated into different experimental groups.
Blinding	Experimenters were blinded during life sciences study design. All subsequent sample processing was done blinded.

Reporting for specific materials, systems and methods

We require information from authors about some types of materials, experimental systems and methods used in many studies. Here, indicate whether each material, system or method listed is relevant to your study. If you are not sure if a list item applies to your research, read the appropriate section before selecting a response.

Materials & experimental systems

n/a	Involved in the study
☒	☐ Antibodies
☒	☐ Eukaryotic cell lines
☒	☐ Palaeontology and archaeology
☐	☒ Animals and other organisms
☒	☐ Clinical data
☒	☐ Dual use research of concern
☒	☐ Plants

Methods

n/a	Involved in the study
☒	☐ ChIP-seq
☒	☐ Flow cytometry
☒	☐ MRI-based neuroimaging

Animals and other research organisms

Policy information about studies involving animals; ARRIVE guidelines recommended for reporting animal research, and Sex and Gender in Research

Laboratory animals	All animal care and experimental protocols were reviewed and approved by the Animal Experimental Ethics Inspection of Southeast University (20240926002)
Wild animals	No wild animals were used in the study
Reporting on sex	No sex information were collected in this study
Field-collected samples	No field collected samples were used in the study
Ethics oversight	All animal care and experimental protocols were approved by the Animal Experimental Ethics Inspection of Southeast University

Note that full information on the approval of the study protocol must also be provided in the manuscript.

Plants

Seed stocks	N/A
Novel plant genotypes	N/A
Authentication	N/A